



# Comparing the Real and Imaginary parts of a Photoacoustic Infrared Spectrum

by

© **Joseline Aimee**

A thesis submitted in partial fulfillment of the requirements for the degree of Bachelor of Science (Honours).

Department of Physics and Physical Oceanography  
Memorial University of Newfoundland

May 2021

St. John's, Newfoundland and Labrador, Canada

# Abstract

Vibrations among atoms in a solid material can be triggered by absorbing infrared light. The energy associated with different kinds of vibrations, such as bending or stretching, are influenced by the types of atoms and their arrangements. Photoacoustic Spectroscopy (PAS) is an experimental technique that allows us to assess what energies of infrared light a solid material can absorb. In this thesis, we focus on implementing mathematical tools and methods on previously collected photoacoustic spectra to manipulate the data in a new way. The goal is to extract the real and imaginary parts of various photoacoustic infrared spectra. Once extracted, we analyze the data to determine whether there are consistent differences (or similarities) between the two parts as we keep the sample the same, but change the photoacoustic detection parameters. We then evaluate which additional terms have to be considered to account for these differences or similarities, and analyze whether they are solely due to instrumentation effects, or if they can provide us with useful information about the structure of our solid sample.

# Acknowledgements

First and foremost, I want to express my gratitude to God Almighty for his grace, faithfulness, and blessings throughout this project and my undergraduate studies.

I would like to express deepest gratitude to my supervisor, Dr. Kristin M. Poduska, for her continuous guidance, patience and compassion. Her willingness to share her knowledge and experience with me is deeply appreciated and I am forever grateful. I would also like to thank Dr. Kirk Michaelian for his help with facilitating my education in photoacoustic spectroscopy. I am honoured to have had the opportunity to work with him on this project.

I would also like to express my gratitude to all members of the Poduska Research Group for laying the foundation for this project, particularly Stephen Campbell for providing the data used in this thesis. Without their support, time, guidance, and encouragement, this project would not have been possible. For the past few years, their mentorship has been a priceless blessing.

I would also like to thank my mother, Francoise Mbanankira. I have been inspired and encouraged by her life journey. Words cannot express or measure how much her advice, motivation, and love have meant to me. For everything she has done for me, I am eternally grateful.

Finally, I would like to thank the Department of Physics and Physical Oceanography for their support.

# Table of contents

Title page	i
Abstract	ii
Acknowledgements	iii
Table of contents	iv
List of tables	vi
List of figures	vii
List of abbreviations	ix
List of symbols	x
<b>1 Introduction</b>	<b>1</b>
1.1 Infrared Radiation for Material Characterization . . . . .	1
1.2 Authorship Statement . . . . .	2
<b>2 Background Information</b>	<b>4</b>
2.1 The Photoacoustic Effect . . . . .	4
2.2 Photoacoustic Detection . . . . .	4
2.2.1 Fourier Transformation . . . . .	7

2.2.2	Phase Correction . . . . .	8
2.3	Data Analysis Approach . . . . .	9
<b>3</b>	<b>Results and Discussion</b>	<b>11</b>
3.1	Photoacoustic Measurements of Calcite . . . . .	11
3.2	Spectra at Different Scan frequencies . . . . .	13
3.2.1	Resonance Effect . . . . .	13
3.2.2	Peak Intensities . . . . .	16
3.2.3	Peak Width and Position . . . . .	17
3.3	No-phase Correction Data . . . . .	17
3.3.1	Spectra at Different Scan frequencies . . . . .	19
3.3.2	Intensity Trend . . . . .	21
3.3.3	Peak Width and Position . . . . .	22
<b>4</b>	<b>Conclusion and Future Work</b>	<b>24</b>
4.1	Conclusion . . . . .	24
4.2	Future Work . . . . .	25
<b>A</b>	<b>Pre-processing procedure</b>	<b>26</b>
<b>B</b>	<b>Sign Change of Peaks</b>	<b>30</b>
	<b>Bibliography</b>	<b>32</b>

# List of tables

3.1	Resonance peak positions for the Gasera PAS-301 cell. Values in the first three columns come from [3]. In the fourth column, the letters "X" denote positions in the spectrum where we expect resonance to interfere with calcite peaks. . . . .	15
3.2	Trend in peak signs for both the real and imaginary components spectra as the scan frequency is increased. Peaks marked with a "*" were not well resolved. . . . .	20
3.3	Relative intensity majority for each scan frequency for each peak. Some peaks do not appear, while others are prominently affected by the resonance effect. Peaks marked with a "*" were not well resolved. . . . .	21

# List of figures

2.1	Schematic diagram of a Michelson interferometer. . . . .	6
2.2	A calcite sample interferogram at 3.0 kHz scan frequency. The center-burst or zero path difference is an area of zero phase difference. . . . .	8
2.3	A graph of the complex plane showing the relationships between the magnitude, $M(\nu)$ , and phase angle, $\theta(\nu)$ , of the photoacoustic signal vector, $P(\nu)$ , and the orthogonal component magnitudes, $R(\nu)$ and $I(\nu)$ . . . . .	9
3.1	A phase-corrected PAS spectrum of a calcite sample collected at a scan frequency of 3.0 kHz. . . . .	12
3.2	PAS spectra of calcite ( $2700\text{ cm}^{-1}$ - $600\text{ cm}^{-1}$ ) at varying scan frequencies. There is usually a decrease in spectral intensity with increasing scan frequency. There appears to be no change in peak position as the scan frequency is increased. . . . .	13
3.3	New and exaggerated peak ( $804\text{ cm}^{-1}$ ) in the 16.0 kHz scan frequency induced by the resonance effect. . . . .	14
3.4	PAS spectra at various scan frequencies in the $\nu_1 + \nu_3$ (a) and $\nu_3$ (b) peak regions. Data that is predominantly affected by resonance is removed from the respective regions. . . . .	16
3.5	Magnitude photoacoustic spectra of a calcite sample at various frequencies in the $1850\text{ cm}^{-1}$ - $1750\text{ cm}^{-1}$ wavenumber region. The $\nu_1 + \nu_4$ combination mode is labeled exhibiting no change in wavenumber position or width as the scan frequency is increased. . . . .	18

3.6	Real (black) and imaginary (red) components of the PAS spectrum of a calcite sample. This data was collected with a 3.0 kHz scan frequency.	19
3.7	Real (black) and imaginary (red) component spectra at 3.0 kHz (left) and 9.0 kHz (right) scan frequencies. A change in sign of the $\nu_4$ peak is observed in both spectra as the scan frequency is increased. . . . .	20
3.8	Magnitude spectra in the $2700\text{ cm}^{-1}$ - $1700\text{ cm}^{-1}$ wavenumber region. The intensities of all of the real component data are made positive and the intensities of all the imaginary component data are made negative.	22
3.9	Magnitude spectrum in the $750\text{ cm}^{-1}$ - $700\text{ cm}^{-1}$ wavenumber region. The $\nu_4$ peak in both the real and imaginary spectra are labeled in its expected location. Intensities are given as arbitrary units because spectra have been shifted and scaled. . . . .	23
3.10	Magnitude spectrum in the $1700\text{ cm}^{-1}$ - $1200\text{ cm}^{-1}$ wavenumber region. The $\nu_4$ peaks in both spectra are labeled in the expected location. Intensities are given as arbitrary units because spectra have been shifted and scaled. . . . .	23
A.1	Computational notebook containing python code employed in this work.	29
B.1	Magnitude spectra for each vibrational mode in the real component spectra. . . . .	31
B.2	Magnitude spectra for each vibrational mode in the imaginary component spectra. . . . .	31

# List of abbreviations

CaCO <sub>3</sub>	Calcite (calcium carbonate)
cm <sup>-1</sup>	inverse centimeters, a unit of energy common in IR spectroscopy
PAS	Photoacoustic Spectroscopy
Im	Imaginary
IR	Infrared
kHz	a unit of frequency common in IR spectroscopy
Mid-IR	Mid-Range Infrared
Re	Real
Res	Resonance
ZPD	Zero Path Difference

# List of symbols

$\nu_1$	symmetric stretching mode of calcite
$\nu_2$ ( $^{12}\text{C}$ )	out-of-plane bending mode of calcite with carbon-12 isotope
$\nu_2$ ( $^{13}\text{C}$ )	out-of-plane bending mode of calcite with carbon-13 isotope
$\nu_3$	asymmetric stretching mode of calcite
$\nu_4$	in-plane bending mode of calcite
$\nu_1 + \nu_3$	combination mode of calcite
$\nu_1 + \nu_4$	combination mode of calcite

# Chapter 1

## Introduction

### 1.1 Infrared Radiation for Material Characterization

A solid material is characterized by the arrangement, type and stoichiometry of its atoms. The atomic vibrations within solids have infrared range energies. This means that a solid will absorb electromagnetic radiation at particular energies that correspond to its own oscillation frequencies [2]. The vibrations are characterized as modes and they include asymmetric stretching, symmetric stretching, wagging, scissoring, twisting and rocking. The wavenumber at which a solid will absorb infrared light is determined by types of atoms and their arrangements. Therefore, materials with the same chemical composition but different atomic arrangements will give rise to different vibrational modes [5, 7]. Accordingly, infrared radiation absorption is a powerful technique used in a wide range of research and disciplines as a material characterization technique.

Photoacoustic Spectroscopy (PAS) is a non-destructive technique that allows the identification of arrangement, type and stoichiometry of atoms without causing damage to the sample being studied. This method utilizes the notion of infrared energy absorption and the propagation of generated thermal waves to produce a photoacoustic spectrum, which is a plot of the measured photoacoustic intensity versus wavenumber ( $4000\text{ cm}^{-1}$  -  $400\text{ cm}^{-1}$ ). The spectrum exhibits peaks that correlate to the infrared activated vibrations within the solid material which in turn is related to the crystal

structure of the material.

The relationship between photoacoustic detection and spectral features are investigated in this work. The real and imaginary components of the photoacoustic spectrum are also extracted and examined, with the objective of determining whether consistent similarities or differences between the two are due to the instrumentation effects or if they can be related to the structure of the solid sample. We hope that information gained in this work can be used with further experiments to identify structural changes in a material.

## 1.2 Authorship Statement

This thesis contains data collected by Stephen Campbell, a student in our research group from Memorial University of Newfoundland's Department of Physics. The experiments were conducted using a Bruker Vertex 70v spectrometer fitted with a PAS-301 photoacoustic cell attachment (Gasera Inc). In his masters thesis [2], Campbell outlines a step-by-step procedure for data collection using PAS method with Bruker's OPUS software. For reference the relevant scan parameters he used to collect the data are listed here.

1. Interferogram is apodized (Blackman-Harris 3-Term apodization function)
2. Interferogram is zerofilled (zerofilling factor of 2)
3. Interferogram is Fourier transformed
4. Spectrum is phase corrected (Mertz phase-correction)

Campbell's thesis describes these parameters in detail, as well as the various scan parameters available on OPUS, but it is not required for this work. However, for subsequent analysis, a thorough understanding of the function of Fourier transformation and phase correction is required, and these parameters will be discussed later in this work.

This data included five different scan frequencies for the same high crystallinity calcite (Alfa Aesar) powder sample, with no repacking between scans. I plotted all of the data and used various programming tools to analyze them from a new perspective.

Our collaborator at Natural Resources Canada (Devon, AB), Dr. Kirk Michaelian, and my supervisor, Dr. Kristin M. Poduska, helped me through the steps of analyzing the data as well as provided comments.

# Chapter 2

## Background Information

### 2.1 The Photoacoustic Effect

The core of photoacoustic spectroscopy is based on turning a sample's absorption of infrared light to sound. The first detection of the photoacoustic effect was made in 1880 when Alexander Graham Bell observed that a material enclosed in a cell emitted audible sound when exposed to a continuous interrupted beam of sunlight [12]. The production of the acoustic signal was a subject of considerable postulation with suggested causes ranging from mechanical motion of the solid to the persistent heating and cooling of the solid by the chopped light [1]. Ultimately, the infrared radiation that is periodically absorbed by the sample is converted into heat and in 1976 a quantitative derivation conducted by Allan Rosencwaig and Allen Gersho concluded that this heat flow from the solid to the surrounding gas is the main source of the acoustic signal [12].

### 2.2 Photoacoustic Detection

Spectra for high crystallinity calcite (Alfa Aesar) were collected with a Bruker Vertex 70v spectrometer fitted with a PA-301 photoacoustic cell attachment (Gasera Inc). The operations of the spectrometer and the procedural details are outlined in this section.

The instrumentation is configured as a Michelson interferometer. A schematic

diagram of the interferometer is shown in Figure 2.1. The data analyzed in this work was collected using rapid scan PAS. The process begins with radiation from an infrared light source traveling to a beam splitter where it is split into two beams with half the initial intensity. One of the beams is directed toward a stationary mirror, while the other is directed towards a moving mirror that scans back and forth at a constant velocity [5]. The stationary and moving mirrors create a path difference between the two beams, resulting in interference. After reflecting on their respective mirrors, the two light beams recombine on the beam splitter, and the combined beams move to the photoacoustic cell, where the solid sample is placed and surrounded by a gas (air).

The beam intensity is modulated at frequency given by:

$$f = \tilde{\nu}v \quad (2.1)$$

where  $\tilde{\nu}$  is the wavenumber of the light in cm and  $v$  is the mirror velocity (scan frequency) in cm/s [8, 9]. There is therefore, a unique modulation frequency corresponding to each wavenumber.

McClelland [8] describes how the PA signal is generated: the infrared beam intensity incident on the sample with intensity  $I_0$ . At a depth  $L$  within the sample, the intensity decays exponentially according to:

$$I = I_0(1 - R)e^{-\alpha L} \quad (2.2)$$

where  $R$  is the fraction of the light that is reflected on the sample's surface and  $\alpha$  is the absorption coefficient of the sample.

Temperature fluctuations occur within the sample as a result of light absorption, resulting in thermal waves that diffuse with a decay coefficient  $a_s$  given by the equation:

$$a_s = (\pi f/D)^{1/2} \quad (2.3)$$

where  $f$  is the modulated frequencies as described above and  $D$  is the thermal diffusivity of the sample. The depth to which the infrared radiation penetrates, also referred to as the thermal diffusion length, is given by the equation:

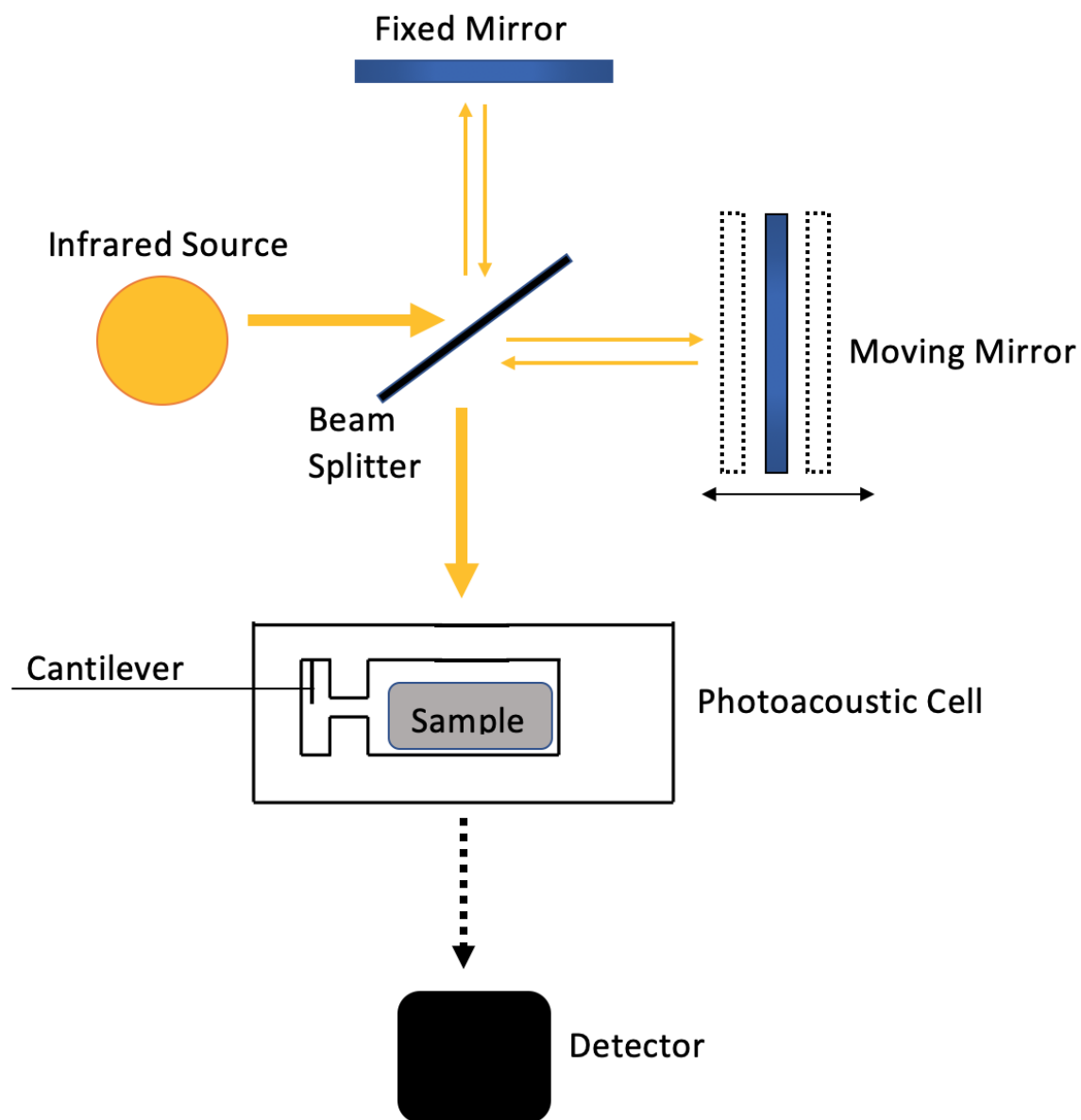


Figure 2.1: Schematic diagram of a Michelson interferometer.

$$L = 1/a_s = (D/\tilde{\nu}v)^{1/2} \quad (2.4)$$

where the substitution  $f = \tilde{\nu}v$  has been made.

The generated thermal waves cause the temperature of the surrounding gas to fluctuate, causing the gas (air) near the sample to expand and contract periodically. Pressure waves in the gas produce an acoustic signal that is detected by a microphone or a microcantilever within the photoacoustic cell [2, 12]. The intensity of the recorded signal is proportional to both the decay of the infrared radiation as it enters the sample and the decay of the thermal waves as they leave the sample [5]. This is described by the equation:

$$I \propto \alpha e^{-(\alpha+a_s)L} \quad (2.5)$$

As described in Equation 2.4, a slower scan frequency ( $\tilde{\nu}$ ) allows the infrared light to penetrate deeper into the sample and leads to an increase in the thermal diffusion length. This in turn results in more heat transferred into the surrounding gas, resulting in higher peak intensities in the spectra [9]. It is therefore the magnitude of the thermal diffusion length that regulates the photoacoustic signal.

### 2.2.1 Fourier Transformation

For a sample spectrum, the solid absorbs some of the infrared light which is converted into heat that diffuses to the surrounding gas resulting in oscillating pressure waves within the cell [9]. The resulting pressure wave is detected by a cantilever and is displayed as an interferogram (see Figure 2.2). A large peak in the middle of the interferogram indicates the maximum interference created by the moving mirror within the interferometer. This center-burst or zero path difference is an area of zero phase difference.

Photoacoustic spectrum measurement parameters encompasses a mathematical transform known as Fourier transformation. This transformation converts the detected data observed on the interferogram from a time-domain into a frequency-spectrum. The output is complex containing a real,  $R(\nu)$ , and imaginary,  $I(\nu)$ , orthogonal components (see Figure 2.3).

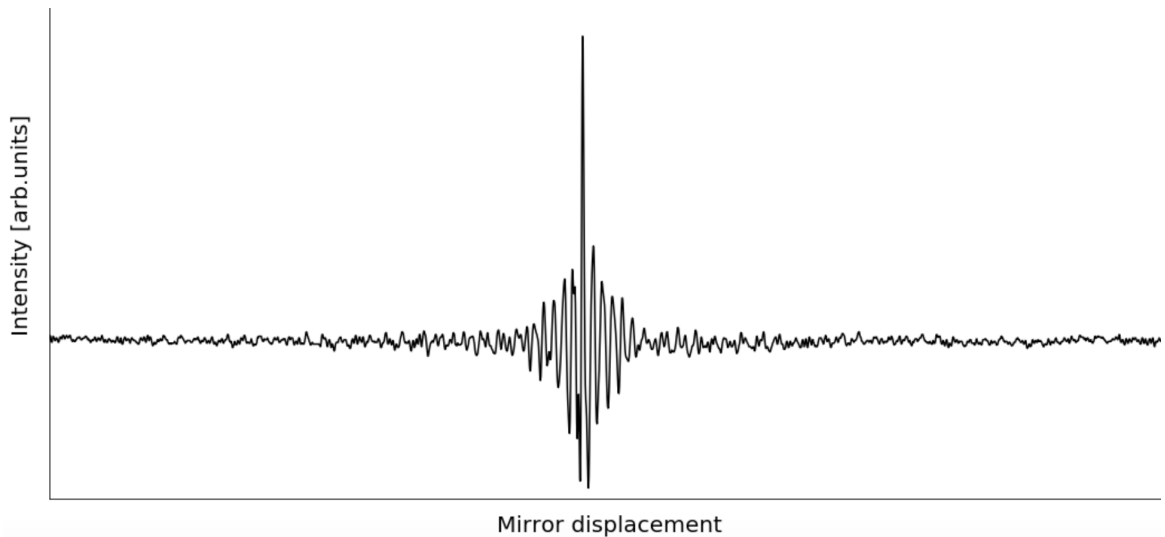


Figure 2.2: A calcite sample interferogram at 3.0 kHz scan frequency. The center-burst or zero path difference is an area of zero phase difference.

These components can be used to calculate the magnitude,  $M(\nu)$ , and phase angle,  $\theta(\nu)$ , according to the relationship:

$$M(\nu) = [R^2(\nu) + I^2(\nu)]^{1/2} \quad (2.6)$$

$$\theta(\nu) = \tan^{-1} \left( \frac{I(\nu)}{R(\nu)} \right) \quad (2.7)$$

### 2.2.2 Phase Correction

A number of defects within the interferometer, such as optical path variations and interferometer misalignment, cause phase errors to appear on the interferogram [11]. This modifies the resulting spectrum to include the instrument's phase response. To account for these errors, phase correction is performed as the final stage of photoacoustic spectral processing [3]. While Bruker's OPUS provides a variety of phase-correction methods, the Mertz phase correction is a common choice for absorption-type experiments on solid samples. The phase corrected spectrum is calculated using the real,  $R(\nu)$ , and imaginary,  $I(\nu)$ , data, as well as the phase angle,  $\theta(\nu)$ , according to the following equation:

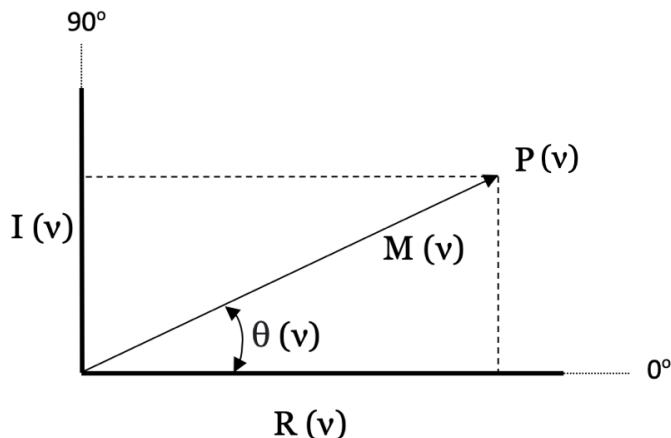


Figure 2.3: A graph of the complex plane showing the relationships between the magnitude,  $M(\nu)$ , and phase angle,  $\theta(\nu)$ , of the photoacoustic signal vector,  $P(\nu)$ , and the orthogonal component magnitudes,  $R(\nu)$  and  $I(\nu)$ .

$$P(\nu) = R(\nu)\cos(\theta(\nu)) + I(\nu)\sin(\theta(\nu)) \quad (2.8)$$

## 2.3 Data Analysis Approach

The core of this thesis is centered on performing preliminary data analysis. The computational and data manipulation software that I used to analyse the data is briefly discussed in this section while the Appendix (A) section of this work includes the step-by-step instructions for reproducing the same analysis.

The data file saved by the spectrometer software contained three sections: the background scan, the interferogram and the Fourier transformed photoacoustic spectrum. To begin, the various sections were extracted and plotted using Quasar, an open-source program based on Python and Orange spectroscopy [4]. Once the photoacoustic spectrum was plotted, the real and imaginary components of the spectrum were also extracted and plotted using the data analysis toolboxes offered in Quasar. However, we found that Quasar has a few hidden data manipulation features that aren't immediately apparent when analysing data. As a result, Bruker's OPUS was used to complete the remaining data extractions and analysis.

Bruker's OPUS (version 7.2) is a proprietary spectra collection and analysis software that interfaces with our IR spectrometer. The interferogram portion of the data

file was transformed into the spectrum using the "Interferogram to Spectrum" function where two new data blocks of the spectrum, SSC R and SSC I, which are the real and imaginary parts, were produced. These data blocks were then plotted in many different ways, using scripts I wrote in the Python programming language.

# Chapter 3

## Results and Discussion

### 3.1 Photoacoustic Measurements of Calcite

In the Mid-IR range ( $4000\text{ cm}^{-1} - 400\text{ cm}^{-1}$ ), calcite ( $\text{CaCO}_3$ ) samples display three main characteristic vibrational absorption peaks that originate from different vibrational modes: the  $\nu_3$ ,  $\nu_2$  and  $\nu_4$  modes. These vibrational modes are due to the motion of the carbonate groups within the unit cell and correspond to asymmetric stretching, out-of-plane bending and in-plane bending respectively. In calcite, the  $\nu_1$  vibrational mode, which corresponds to symmetric stretching, is not IR active; however, modes corresponding to a combination of the  $\nu_1$  and other vibrational modes do occur. The motion of the carbon atom dominates the  $\nu_3$  and  $\nu_2$  vibrational modes while the motion of the oxygen atoms contribute most to the  $\nu_1$  and  $\nu_4$  modes [13].

The phase-corrected photoacoustic spectrum of a high crystallinity calcite (Alfa Aesar) powder sample is shown in Figure 3.1. The data was obtained using a Mertz phase correction with a scan frequency of 3.0 kHz.

The three infrared-active vibrations modes described above are labelled. The  $\nu_3$  peak is broad in width and appears to be a superposition of at least two constituent peaks. It has an observed wavenumber position of  $1453\text{ cm}^{-1}$ , however the reported position of this peak varies between works and ranges between  $1400\text{ cm}^{-1}$  and  $1440\text{ cm}^{-1}$ . Weak peaks that are not related to the sample are also observed in the spectrum, mainly  $\text{H}_2\text{O}$  in the  $4000\text{ cm}^{-1} - 3600\text{ cm}^{-1}$  and  $1600\text{ cm}^{-1}$  wavenumber ranges, as well as the  $\text{CO}_2$  doublet at  $2349\text{ cm}^{-1}$ . McClelland [8] states that the presence of

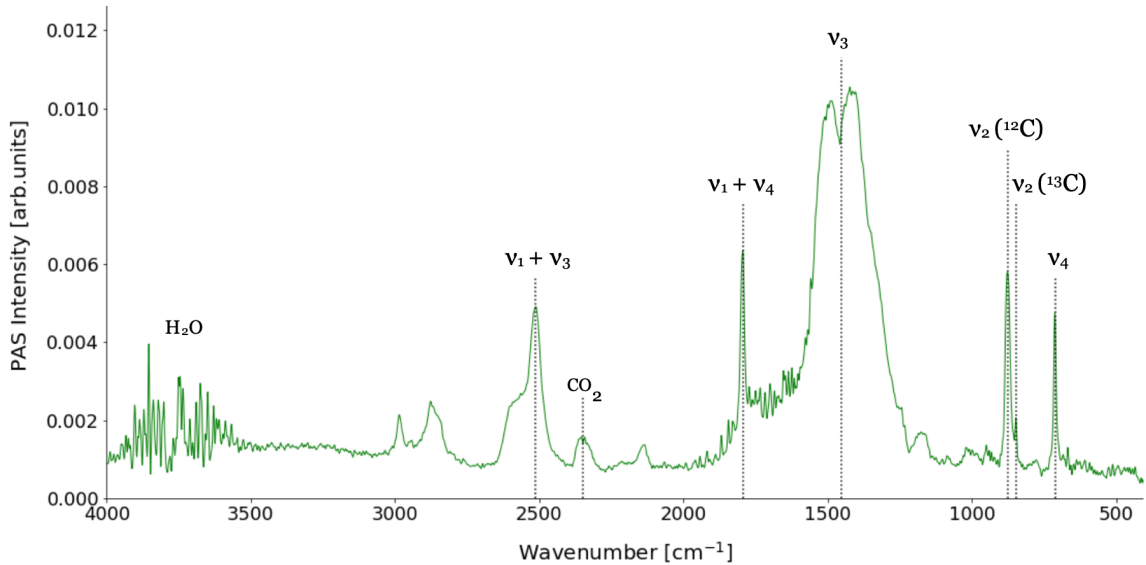


Figure 3.1: A phase-corrected PAS spectrum of a calcite sample collected at a scan frequency of 3.0 kHz.

vapour and gas in both the PAS optical path and the photoacoustic detector may be the cause of moisture and CO<sub>2</sub> bands in PAS spectra. The water and CO<sub>2</sub> peaks are not surprising because the spectra analyzed in this thesis were collected in ambient conditions (in air).

PAS spectra of calcite obtained by Poduska and Xu [14] report the presence of peaks corresponding to a combination of vibrational modes, mainly  $\nu_1 + \nu_4$  at 1800 cm<sup>-1</sup> and  $\nu_1 + \nu_3$  at 2500 cm<sup>-1</sup>. The peak with wavenumber position 1794 cm<sup>-1</sup> in the displayed PAS spectrum is in good agreement with the reported  $\nu_1 + \nu_4$  peak while the peak in position 2512 cm<sup>-1</sup> is in good agreement with the reported  $\nu_1 + \nu_3$  peak. A weak absorbance feature on the low-end wavenumber region of the  $\nu_2$  peak is also worth noting. The origin of this weak features has been the subject of various works of research with many suggesting that it is also due to the combination of vibrational modes. However, a joint experimental and theoretical study by Xu et al. (2018) utilizes isotope substitution effect to ultimately assign this peak to the <sup>13</sup>C isotope [13].

## 3.2 Spectra at Different Scan frequencies

The phase-corrected PAS spectrum of calcite is shown in Figure 3.2 at five different scan frequencies: 3.0 kHz, 9.0 kHz, 10.0 kHz, 16.0 kHz, and 18.0 kHz. Peaks remain at the same wavenumber positions, however peak intensities decrease as the scan frequency is increased. Furthermore, there appears to be a variation in general peak shape, width, and the emergence of new and exaggerated peaks as the scan frequency is increased.

A decrease in intensity is expected because previous studies [8, 9] have shown that as the scan frequency is increased, the penetration depth of infrared radiation decreases, resulting in a decrease in overall intensity signal. However, as shown in Figure 3.2, this observation does not extend to all peaks.

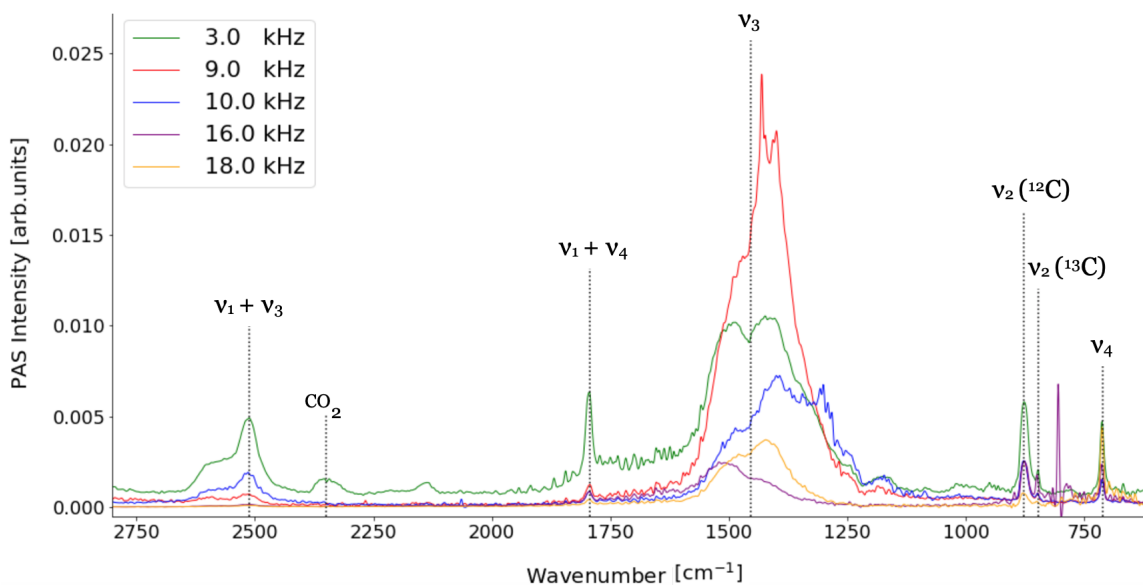


Figure 3.2: PAS spectra of calcite ( $2700 \text{ cm}^{-1} - 600 \text{ cm}^{-1}$ ) at varying scan frequencies. There is usually a decrease in spectral intensity with increasing scan frequency. There appears to be no change in peak position as the scan frequency is increased.

### 3.2.1 Resonance Effect

At different scan frequencies, we also observe that new exaggerated peaks with higher relative intensities appear in the spectrum. Figure 3.3 shows such peak, which is seen

at  $804\text{ cm}^{-1}$  in the 16.0 kHz scan frequency. We believe these peaks are solely due to the resonance effect.

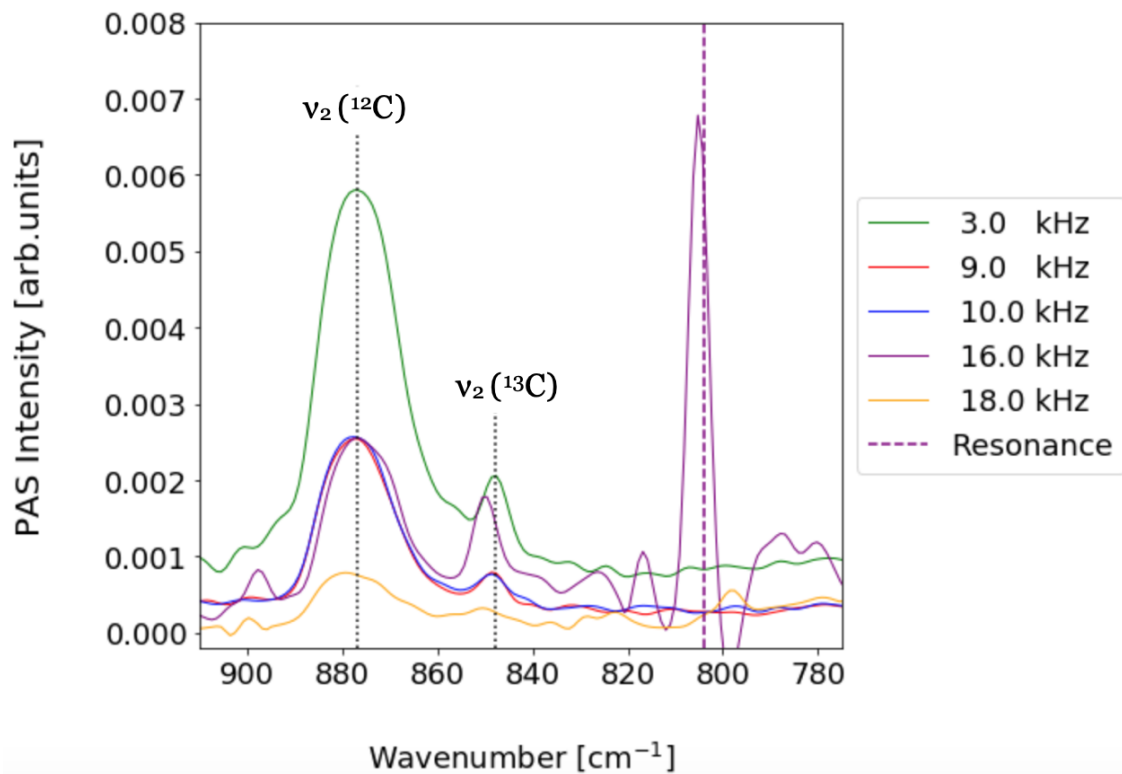


Figure 3.3: New and exaggerated peak ( $804\text{ cm}^{-1}$ ) in the 16.0 kHz scan frequency induced by the resonance effect.

In her thesis, Dusseault [5] examines the potential sources of resonance within the PA-301 photoacoustic cell in depth. She estimates the resonant frequency with rough calculations and concludes that the PA-301 photoacoustic cell, modelled as a single chamber Helmholtz resonator, was in the right range to explain the unusual PAS step-scan spectra obtained in her experiments. Formally, performing Fourier transformation on the interferogram creates a noise-related resonance effect to occur inside the photoacoustic cell. In each experiment, the frequency of the moving mirror comes close to matching the resonances within the photoacoustic cell [5]. This causes exaggerated peaks to emerge in the spectrum that are not related to the sample, which may jeopardise the accuracy of the data when analyzed. Fortunately, peaks on the PAS spectrum that correspond to activated vibrational modes occur in unique and constant wavenumber locations, making it possible to differentiate between peaks caused by the resonance effect and peaks caused by vibrational modes within the

Scan frequency	Resonance position ( $\text{cm}^{-1}$ )		Interfere with calcite peaks
	for 820 Hz	for 1640 Hz	
3.0 kHz	4319	8637	X
5.0 kHz	2591	5182	
7.0 kHz	1851	3702	
9.0 kHz	1440	2879	X
10.0 kHz	1296	2591	X
11.0 kHz	1178	2356	
13.0 kHz	997	1993	
15.0 kHz	864	1727	
18.0 kHz	720	1440	X

Table 3.1: Resonance peak positions for the Gasera PAS-301 cell. Values in the first three columns come from [3]. In the fourth column, the letters "X" denote positions in the spectrum where we expect resonance to interfere with calcite peaks.

sample. Peaks on the spectrum that occur based on the environment in which the data is collected, such as moisture ( $\text{H}_2\text{O}$ ) or carbon dioxide ( $\text{CO}_2$ ), can also be distinguished by their estimated wavenumber locations. Unexpected peaks can be characterized by the resonance effect or other instrumentation contributors that must be accounted for.

The reported resonance position (in  $\text{cm}^{-1}$ ) by the Poduska Research Group are displayed in the first three columns of Table 3.1 for different scan frequencies (in kHz) within the Gasera PA-301 photoacoustic cell. From their results, we see that the resonance that interferes with the calcite peaks shifts its location at different scan frequencies. That is, cell resonance in wavenumbers occurs at various locations per scan frequency [3]. The reported resonance positions for the 9.0 kHz and 10 kHz scan frequencies directly overlap the  $\nu_3$  peak ( $1453 \text{ cm}^{-1}$ ). In the 18.0 kHz scan frequency, the reported resonance position location overlaps the  $\nu_4$  peak ( $712 \text{ cm}^{-1}$ ).

Although the exaggerated peak observed in the 16.0 kHz scan frequency does not directly overlap the  $\nu_2$  peaks (see Figure 3.3), the Poduska Research Group suggest that the effects of resonance disrupts a wide range of wavenumbers rather than a single wavenumber position [3]. Peaks corresponding to IR active vibrational modes that are influenced by resonance lack the certainty of accurate sample information. This means that each wavenumber region containing peaks corresponding to vibrational modes must be analysed separately, with the resonance-affected data being omitted prior to analysis, although they can be used to obtain alternative information in future

studies.

### 3.2.2 Peak Intensities

As discussed above, we expect for the PAS signal to decrease as the scan frequency is increased (see Section 2.2). Closer examination of each wavenumber region containing peaks corresponding to vibrational modes reveals that this trend is not necessarily true for all peaks. For instance, the  $\nu_1 + \nu_3$  peak ( $2512 \text{ cm}^{-1}$ ) has a higher relative intensity value in the 10 kHz scan frequency than in the 9.0 kHz scan frequency. The  $\nu_3$  peak ( $1453 \text{ cm}^{-1}$ ) also shows unusual intensity trend. This peak has a higher relative intensity in the 18.0 kHz scan frequency than in the 16.0 kHz scan frequency. These observations are displayed in Figure 3.4.

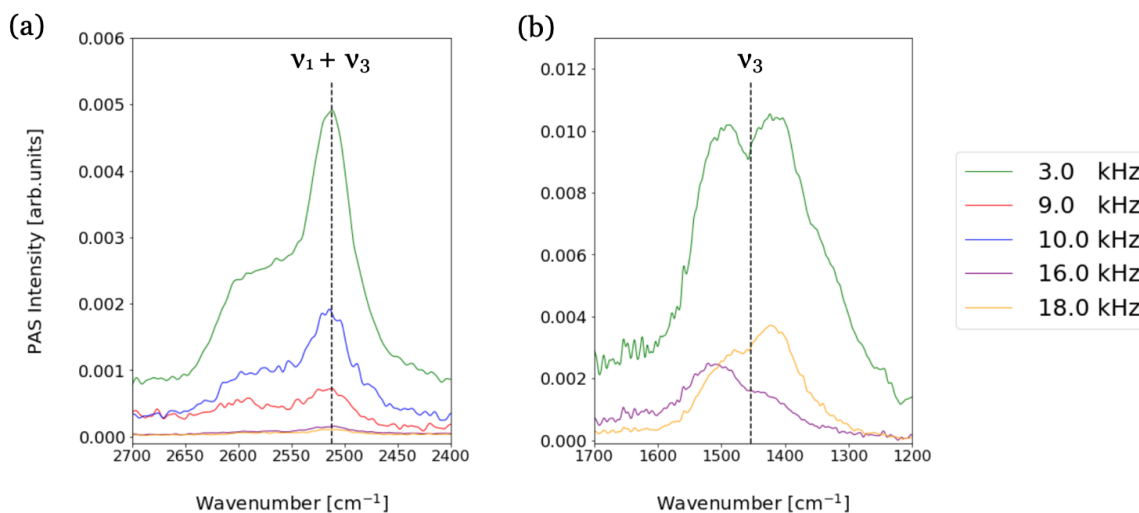


Figure 3.4: PAS spectra at various scan frequencies in the  $\nu_1 + \nu_3$  (a) and  $\nu_3$  (b) peak regions. Data that is predominantly affected by resonance is removed from the respective regions.

The  $\nu_3$  peak corresponds to asymmetric stretching of the carbonate unit. Throughout all scan frequency results, we observe that this peak tends to split into two halves with slightly different relative intensity values. The  $\nu_1 + \nu_3$  occurs at a higher frequency, containing some of the  $\nu_3$  vibration's energy. The weak shoulder in its high wavenumber tail might be accredited to the two halves in the  $\nu_3$  peak. However, at the time of this work, direct speculations cannot be made. The intensity trend of these peaks are significant and complex. Further work is required to understand the

reasoning of these behaviors and how they correlate to the sample.

### 3.2.3 Peak Width and Position

To determine whether the peaks are changing in width or wavenumber position as the scan frequency is increased, the peak intensities are made similar in magnitude. The data is scaled using the peak intensities from the lowest scan frequency analysed in this review, 3.0 kHz. The results reveal that the widths of each peak does not change. This is displayed in Figure 3.5 for the  $\nu_1 + \nu_4$  peak. The lack of peak shift in the result also indicates that peak positions do not change as scan frequency is increased.

## 3.3 No-phase Correction Data

While the effects of changing the scan frequency can be observed in the phase-corrected PAS spectrum, a discussion of the spectrum can be enhanced by considering its real (even function) and imaginary (odd function) components.

By not completing a phase-correction on the interferogram, the optical effects within the interferometer are acknowledge and the data is instead stored as in its real,  $R(\nu)$ , and imaginary,  $I(\nu)$ , components that result from performing Fourier transformation. Figure 3.6 displays the real (black) and imaginary (red) components of the PAS obtained at a scan frequency of 3.0 kHz. The three main vibrational modes ( $\nu_4$ ,  $\nu_2$  and  $\nu_3$ ) as well as the combinations modes ( $\nu_1 + \nu_4$ ,  $\nu_1 + \nu_3$ ) and the peak due to the  $^{13}\text{C}$  isotope ( $848\text{ cm}^{-1}$ ) are exhibited in both spectra with the same peak positions. At this scan frequency, the real spectrum is most similar to the PAS spectrum (see Figure 3.1). This is to be expected because the real spectrum contains the majority of the photacoustic intensity [10].

Figure 3.6 also reveals new and interesting information. For instance, peaks in the real component spectrum tends to be broader in width. Second, the relative intensities of both spectra are significantly different. In the imaginary spectrum, the relative intensity values are lower. Finally, some peaks in the imaginary spectrum, such as the  $\nu_4$  ( $712\text{ cm}^{-1}$ ) peak, have a negative sign.

The objective of subsequent analysis is to determine whether these similarities and

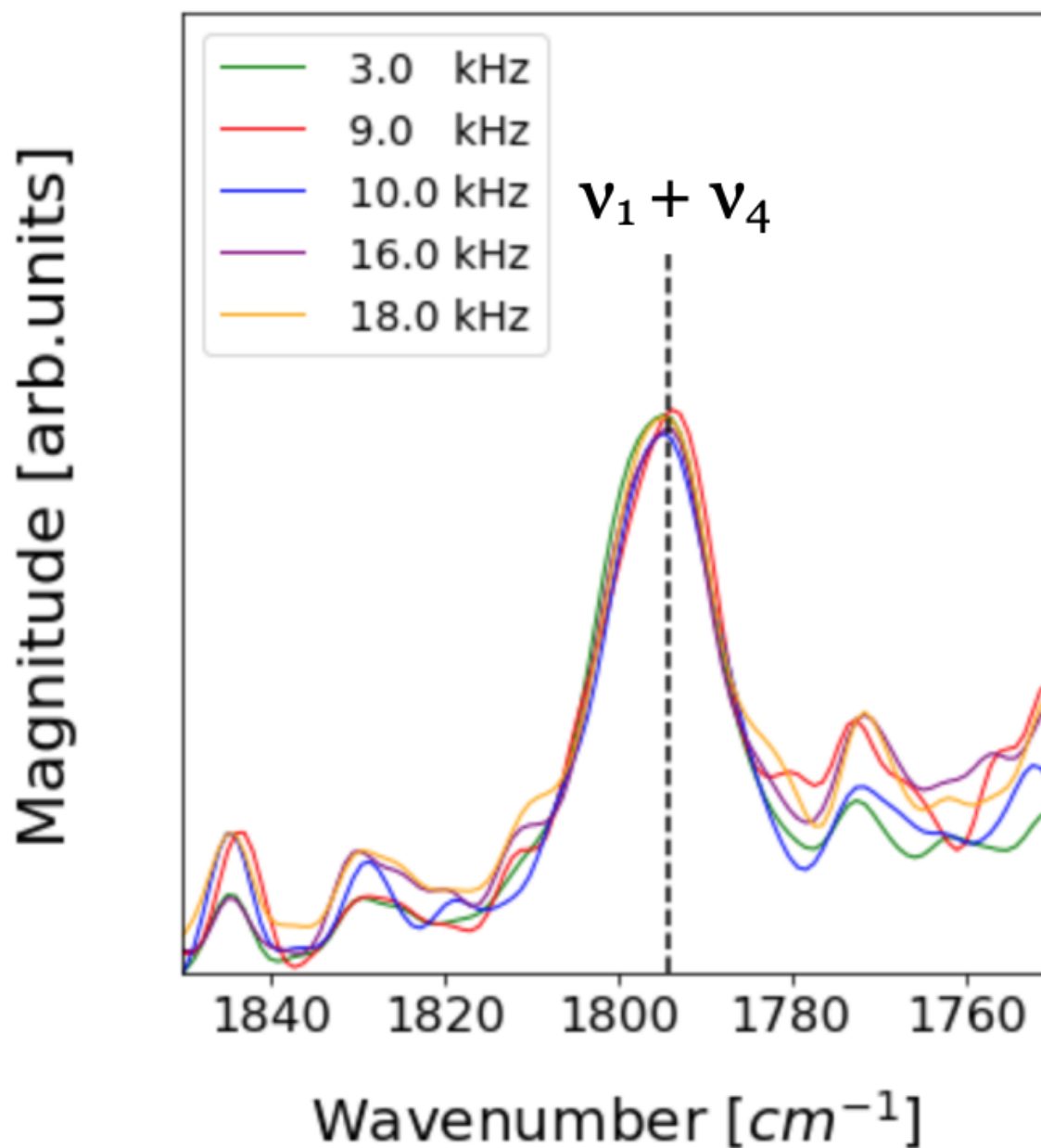


Figure 3.5: Magnitude photoacoustic spectra of a calcite sample at various frequencies in the  $1850\text{ cm}^{-1}$ -  $1750\text{ cm}^{-1}$  wavenumber region. The  $\nu_1 + \nu_4$  combination mode is labeled exhibiting no change in wavenumber position or width as the scan frequency is increased.

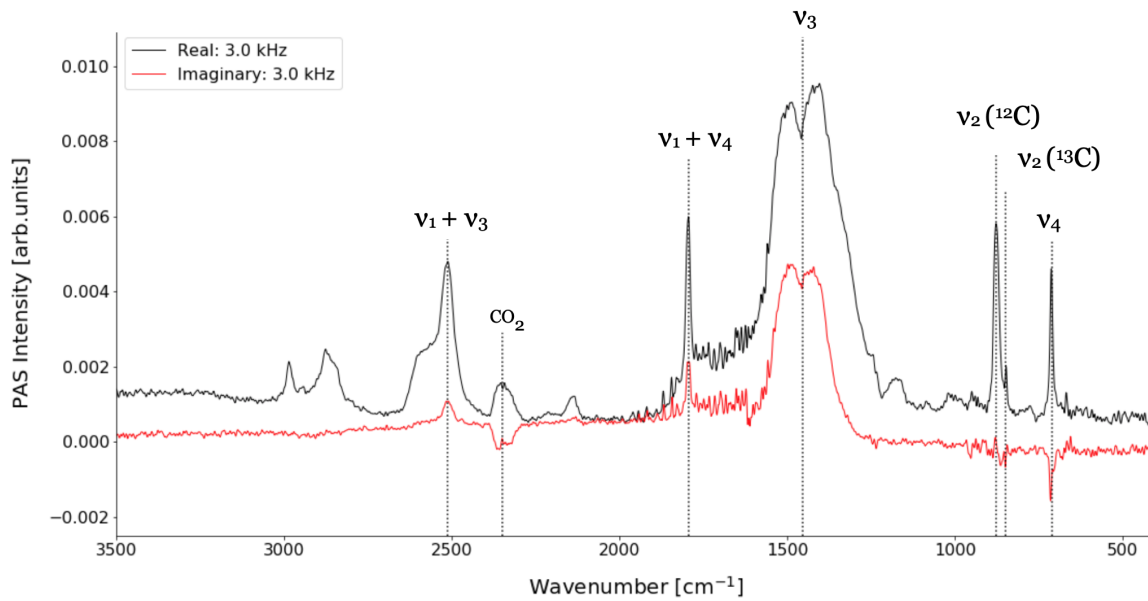


Figure 3.6: Real (black) and imaginary (red) components of the PAS spectrum of a calcite sample. This data was collected with a 3.0 kHz scan frequency.

difference between the real and imaginary spectra are consistent. To do so, we look for variations in peak positions, heights, and widths as the sample is kept the same but the scan frequency is changed.

### 3.3.1 Spectra at Different Scan frequencies

The first observation when the scan frequency is increased is the change in peak signs in both the real and imaginary spectra. Figure 3.7 demonstrates this for the  $\nu_4$  peak. The real component spectrum correspond to the even functions, which can be represented by sums of cosines waves. While the imaginary component spectrum correspond to odd functions, which can be represented by sums of sine waves. It is generally understood that both cosine and sine waves will oscillate between a negative and a positive interval when plotted. As a result, the gradual change in sign of these peaks as the scan frequency is gradually increased is not unexpected. However, this is behaviour that warrants more attention.

Scan frequency	$\nu_1 + \nu_3$		$\nu_1 + \nu_4$		$\nu_3$		$\nu_2 (^{12}\text{C})$		$\nu_2 (^{13}\text{C})$		$\nu_4$	
	Re	Im	Re	Im	Re	Im	Re	Im	Re	Im	Re	Im
3.0 kHz	+	+	+	+	+/+	+/+	+	+	+	-	+	-
9.0 kHz	N/A	N/A	-	*	Res	Res	-	+	-	+	-	+
10.0 kHz	*	*	+	-	Res	Res	-	+	-	+	-	+
16.0 kHz	*	N/A	-	N/A	-/-	*	Res	Res	Res	Res	-	*
18.0 kHz	N/A	N/A	*	-	-/-	+/+	-	-	*	*	Res	Res

Table 3.2: Trend in peak signs for both the real and imaginary component spectra as the scan frequency is increased. Peaks marked with a "\*" were not well resolved.

Table 3.2 provides a summary of these observations and it includes the signs of both peaks that comprise the  $\nu_3$  peak. In certain cases, peaks in one spectrum (Re or Im) have no amplitude or are poorly resolved, making it difficult to ascertain whether or not a peak occurs. A "N/A" or a "\*" is used in these cases, respectively. Peaks distorted by the resonance effect are not taken into account for information and are labelled "Res" in the table.

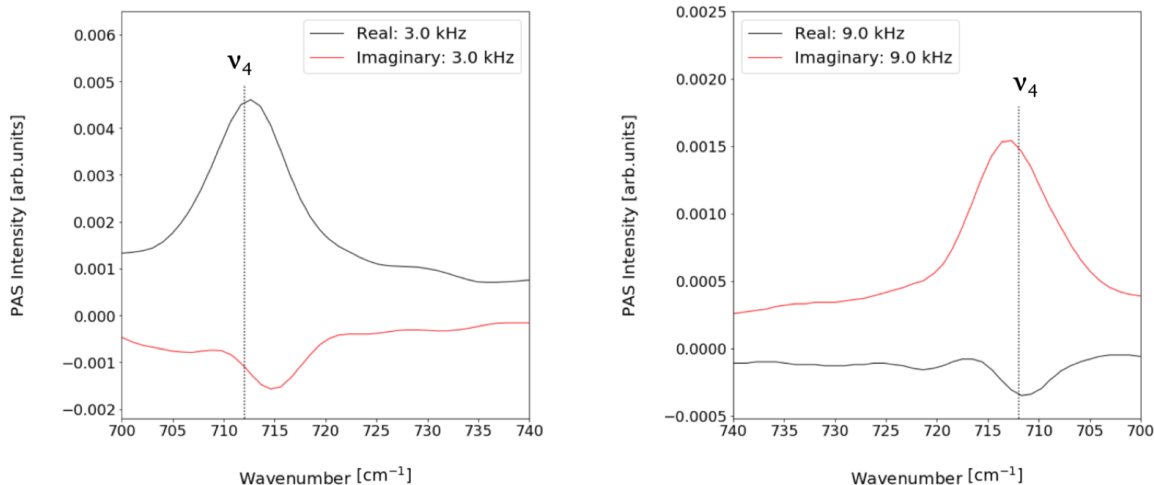


Figure 3.7: Real (black) and imaginary (red) component spectra at 3.0 kHz (left) and 9.0 kHz (right) scan frequencies. A change in sign of the  $\nu_4$  peak is observed in both spectra as the scan frequency is increased.

We also observe that the amplitude of certain peaks varies between the real and imaginary spectra as the scan frequency is increased. That is, some peaks have a greater intensity in the imaginary spectrum than in the real spectrum, and vice versa. This can be seen in Figure 3.7 for the  $\nu_4$  where the majority of the signal is contained

Scan frequency	$\nu_1 + \nu_3$	$\nu_1 + \nu_4$	$\nu_3$	$\nu_2$ ( $^{12}\text{C}$ )	$\nu_2$ ( $^{13}\text{C}$ )	$\nu_4$
3.0 kHz	Re	Re	Re	Re	Re	Re
9.0 kHz	N/A	Re	Res	Re	Re	Im
10.0 kHz	*	Im	Res	Re	Re	Im
16.0 kHz	N/A	Re	Re	Res	Res	Im
18.0 kHz	Re	Im	Re	Im	Re	Res

Table 3.3: Relative intensity majority for each scan frequency for each peak. Some peaks do not appear, while others are prominently affected by the resonance effect. Peaks marked with a " \* " were not well resolved.

in the real spectrum at 3.0 kHz scan frequency, but in the 9.0 kHz scan frequency the majority of the signal is contained in the imaginary spectrum. These observations are summarized in Table 3.3.

### 3.3.2 Intensity Trend

For a comprehensive understanding of what changes and to what extent for various scan frequencies, the magnitude of the real component spectra are compared to the inverse magnitude of the imaginary component spectra. To achieve this, the intensities of all of the real data are made positive and the intensities of all the imaginary data are made negative. Figure 3.8 shows the results in the  $2700\text{ cm}^{-1}$  -  $1700\text{ cm}^{-1}$  wavenumber region, where the  $\nu_2$  peaks in the 9.0 kHz and 10 kHz scan frequencies are made positive in the real component spectra by multiplying their intensity data by negative one, and the  $\nu_2$  peaks in the 3.0 kHz and 9.0 kHz scan frequencies are made positive in the imaginary component spectra using the same method.

As described in Equation 2.4, a higher scan frequency results in less infrared light penetration into the sample. This leads to a decrease in thermal diffusion length resulting in reduced peak intensities in the spectrum. Although this trend can be seen in the majority of the peaks in the data studied in this thesis, it is not true for all of them. For instance, in Figure 3.8 the  $\nu_1 + \nu_3$  peak in the imaginary component spectra has a greater relative intensity in the 10.kHz scan frequency than in both the 3.0 kHz and 9.0 kHz scan frequencies. Usual intensity trend can also be seen in both the real and imaginary spectra the  $\nu_1$  peak. In this case, the 18.0 kHz scan frequency has a greater relative intensity than the 16.0 kHz scan frequency.

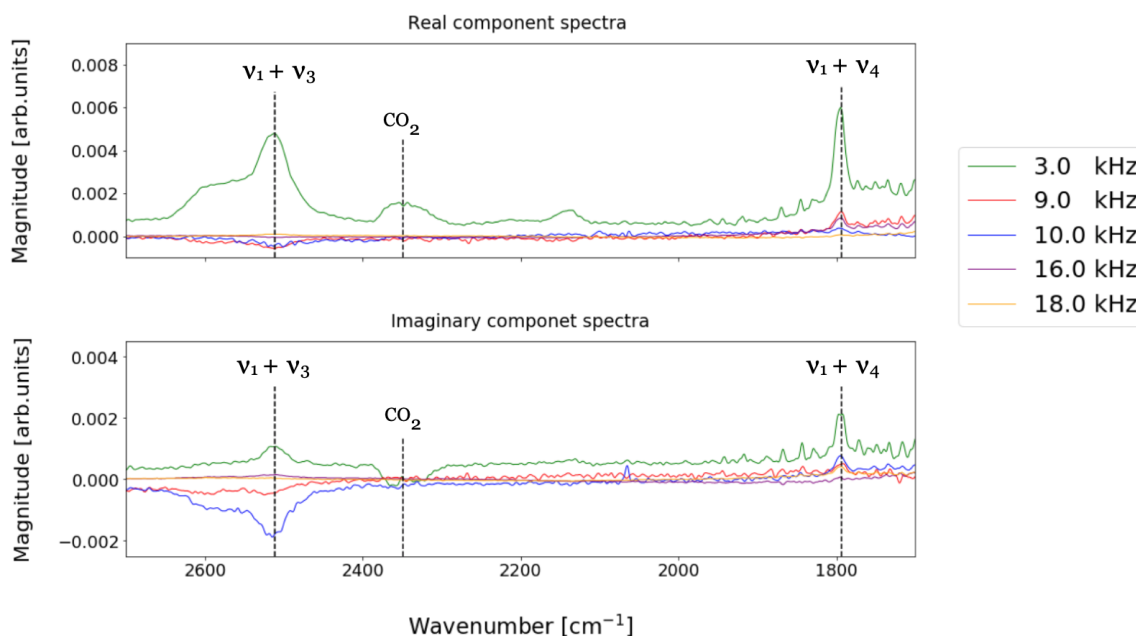


Figure 3.8: Magnitude spectra in the  $2700 \text{ cm}^{-1}$  -  $1700 \text{ cm}^{-1}$  wavenumber region. The intensities of all of the real component data are made positive and the intensities of all the imaginary component data are made negative.

### 3.3.3 Peak Width and Position

By normalizing the peak intensities, we observe that width are not changing for any of the peaks. Figure 3.9 depicts this for the  $\nu_4$  peak in both real and imaginary spectra.

In both the real and imaginary spectra, we find that adjusting the scan frequency has no effect on peak position. The  $\nu_3$  peak, however, is more complicated (see Figure 3.10). As mentioned previously, not only does the precise position of this peak differ between works, but it is also evident from this thesis that this peak splits into two. Further work is needed for a concrete understanding of these findings and what they may mean in relation to the sample.

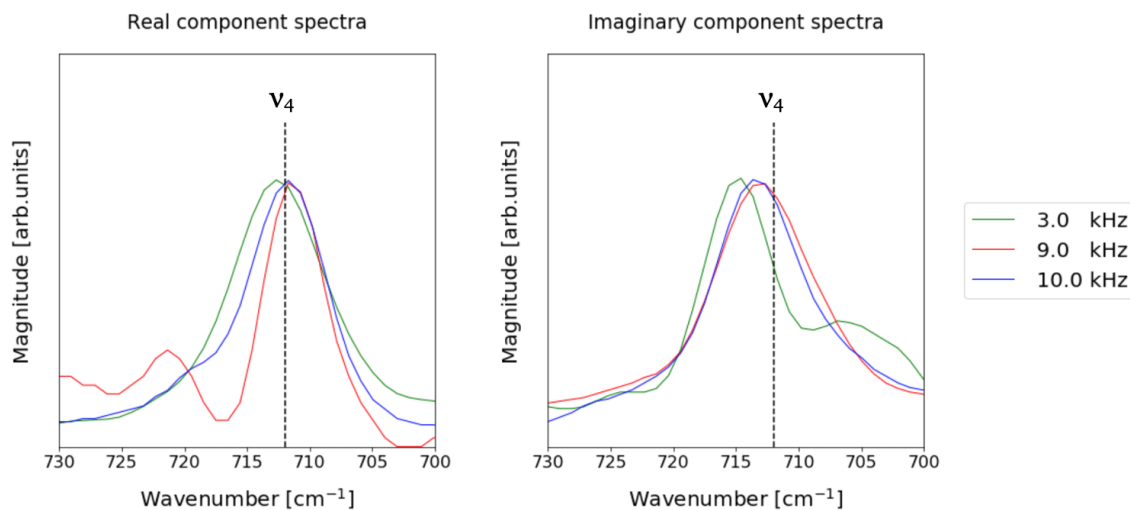


Figure 3.9: Magnitude spectrum in the  $750\text{ cm}^{-1} - 700\text{ cm}^{-1}$  wavenumber region. The  $\nu_4$  peak in both the real and imaginary spectra are labeled in its expected location. Intensities are given as arbitrary units because spectra have been shifted and scaled.

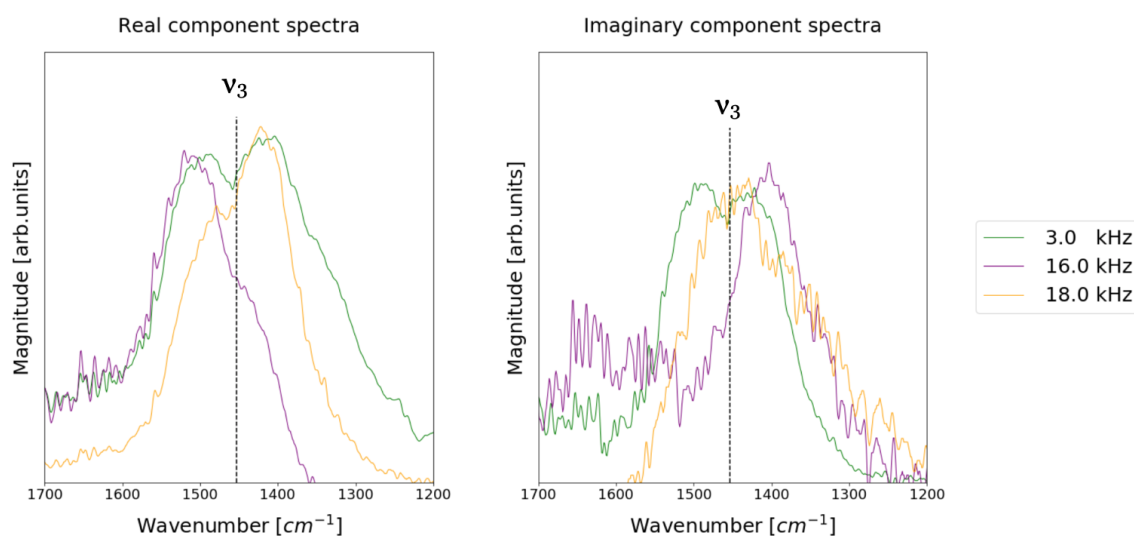


Figure 3.10: Magnitude spectrum in the  $1700\text{ cm}^{-1} - 1200\text{ cm}^{-1}$  wavenumber region. The  $\nu_3$  peaks in both spectra are labeled in the expected location. Intensities are given as arbitrary units because spectra have been shifted and scaled.

# Chapter 4

## Conclusion and Future Work

### 4.1 Conclusion

The PAS measurement sequence typically involves performing a phase correction on the data once the interferogram has been Fourier transformed. This removes the complex plane and returns a spectrum that is entirely in the real plane (see Figure 2.3). As a result, the real and imaginary components of the spectrum are rarely assessed separately. In this work, we have used computational analysis to analyze these two components in depth. Specifically, we have analyzed the similarities and difference between the two components at different scan frequencies.

As the scan frequency is increased, the results show the peak's positions and peak width do not change. However, their signs and amplitudes do change. In particular, while some peaks have remained positive, others have shifted to the negative. Furthermore, the peak's intensity shifts between the real and imaginary component spectra as the scan frequency is increased. This observation particularly is interesting because previous studies [10] have stated that the majority of the PAS intensity is found in the real spectrum. However we have found that this is not the case for all scan frequencies.

Significant observations made in this work include:

- The  $\nu_3$  peak splits into two halves, each with a different relative intensity. In addition, the majority of this peak's intensity varies between the real ( $R(\nu)$ ) and

the imaginary ( $I(\nu)$ ) component spectra.

- As the scan frequency increased, the intensity trend of the  $\nu_1 + \nu_3$  peak and the  $\nu_3$  peak does not decrease with increasing scan frequency, as we would expect.
- Peaks in both the real and imaginary spectra change sign as the scan frequency is increased. The amplitude of some peaks is near zero or not resolved. These observations are summarized in Appendix B.

## 4.2 Future Work

In order to gain a better understanding of the findings made in this thesis, I mention in the previous sections that future work might include:

- Check for reproducibility by collecting data on other calcite samples.
- An investigation of the  $\nu_3$  peak. Identifying the reason this peak splits into two and why only a portion of it is in the imaginary component spectrum.
- The phase angle of the photoacoustic signal also contains valuable compositional information. Phase angle analysis would allow for continuous monitoring of changes in both peak direction and real/imaginary intensities majority. This kind of analysis is not common in the literature, but there is one example for a material that is very different from calcite (see Figure 6 in [10]).

These tasks would help improve our understanding of phase differences in photoacoustic FTIR measurements.

# Appendix A

## Pre-processing procedure

The pre-processing procedure I used to analyze the PAS data can be broken into three major components: loading the original data files into OPUS, exporting and saving the different data blocks as new files and importing these new files into a python code. A step-by-step description of this procedure is outlined in this section while an in-depth look of the various measurement parameters available in OPUS can be obtainable elsewhere [6].

### Extracting Data Blocks Files

1. Click on the View menu and select Toolbar. You will then be provided with a window where you can customize your icons. Drag the Manipulate toolbar's "Interferogram to Spectrum" function to the top of your menu bar.
2. Load your OPUS data file using the Load File command from the File menu. In the browser window, the file name, data blocks, and file status information will be displayed.
3. Click the interferogram data block that is part of the spectrum file. The data block will become colored indicating that the interferograms has been selected and is displayed within the spectrum window.
4. Click the "Interferogram to Spectrum" function and select the "Phase Correction" tab.

5. From the pull-down menu, select "No/Save Complex Data." Instead of being phase corrected, the data will be transformed into a complex form and stored as real and imaginary parts.

At this stage, the spectrum should have two new data blocks in the OPUS browser: SSC R and SSC I, which correspond to the real and imaginary parts of the spectrum, respectively. The data blocks will become coloured when clicked and the corresponding spectrum will display on the spectrum window.

## Baseline Correction

A baseline correction is typically applied on a spectrum prior to analysis such as peak picking. In this approach uneven amplitudes throughout the spectrum are re-established on a new baseline. OPUS provides both automatic and interactive mode options for these circumstances. However, a baseline correction lead to a distortion of the negative intensities that occasionally occur in the imaginary component spectrum. This limitation of accuracy in the spectra information meant that a baseline correction was unreliable in some regions. Therefore, a baseline correction was not performed on the data for subsequent analysis.

## Exporting the Data Blocks Files

1. Select the the real (SSC R) block and click the "Save File As" command. Choose an appropriate file name as well as the file PASTh on the Select Files tab.
2. Click on the mode tab and select "Pirouette.DAT" output format. The data file will be saved as a DAT file, which can then be imported into Python for further analysis.
3. Click on the "Save" button to save the spectrum file.
4. To ensure that the data has been saved correctly, open it in NotePASd text editor, where it should appear as columns.
5. Repeat this process for the Imaginary (SSC I), interferogram and PAS data blocks.

Optionally, one can select the whole data file and select the "Save all" button in the Mode command to save all data blocks simultaneously. Repeat these steps for each data files that is to be analyzed.

## Importing data files in Python

Once the data files have been saved, one can begin to import the data into python. The python code developed in this work can be used to analyze more spectra, other samples, or other data under similar conditions. While python requires that a set of functions and plotting libraries, such as Matplotlib, be imported first, this section summarises the basic steps for importing the data.

1. To load the data file, choose an appropriate name and use "np.loadtxt('fileName.dat', delimiter=',')" function to download the file.
2. The DAT file should contain (at least) two columns of data corresponding to the wavenumber and intensity. These columns are specified by choosing an appropriate name and using basic slice syntax on the data file.
3. The data is then plotted using the "plt.plot(wavenumber,intensity)" function. The wavenumber will be displayed on the x-axis, while the pressure will be displayed on the y-axis.
4. vertical lines across the axes of the plot can be added by using the "axvline(x=0, ymin=0, ymax=1)" function where the x position in data coordinates of the vertical line is specified in the first entry. This function was used to show the wavenumber position of vibrational modes in this study.
5. Repeat these steps for each data files that is to be analyzed.

Multiple series can be plotted by importing the "plt.plot(x,y)" function and the respective variables into the same cell. In addition, the python script developed in this thesis offers the possibility to perform mathematical calculations on the data files.

```

#1) Load the data files:
ThreekHz_RealData_OPUS = np.loadtxt('Real_Parameterized_20191220_RS-3.0kHz_PAS_MIR_smc_ca
lcite_Res4_scan2min_exgain0.2_gain4,4_phase8_mertz.dat', delimiter=',')
ThreekHz_ImagData_OPUS = np.loadtxt('Imag_Parameterized_20191220_RS-3.0kHz_PAS_MIR_smc_ca
lcite_Res4_scan2min_exgain0.2_gain4,4_phase8_mertz.dat', delimiter=',')
#-----
#2) columns of the data file are specified:

#Real data:
wavenumber_ThreekHz_RealData_OPUS = ThreekHz_RealData_OPUS[:,0] #First column
Real_ThreekHz_RealData_OPUS = ThreekHz_RealData_OPUS[:,1] #Second column

#Imaginary data:
Wavenumber_ThreekHz_ImagData_OPUS = ThreekHz_ImagData_OPUS[:,0] #First column
Imaginary_ThreekHz_ImagData_OPUS = ThreekHz_ImagData_OPUS[:,1] #Second column
#-----
#3) Plot the data : plt.plot(First column,Second column)

plt.figure(figsize=(15,4)) #Figure size

#Real data:
plt.plot(wavenumber_ThreekHz_RealData_OPUS, Real_ThreekHz_RealData_OPUS, color = 'black'
, label = 'Real: 3.0 kHz', linewidth = 1) #(x,y), linewidth = width of line plot
#imaginary data
plt.plot(Wavenumber_ThreekHz_ImagData_OPUS, Imaginary_ThreekHz_ImagData_OPUS, color = 're
d', label = 'Imaginary: 3.0 kHz' , linewidth =1) #(x,y)

#Vibrational modes
plt.axvline(x=712, ls=':', color='black', ymax = 0.65) #line showing: x = 712cm-1
plt.axvline(x=848, ls=':', color='black', ymax = 0.75) #line showing: x = 847 cm-1
plt.axvline(x=877, ls=':', color='black', ymax = 0.75) #line showing: x = 877 cm-1
plt.axvline(x=1453, ls=':', color='black', ymax = 1) #line showing: x = 2512cm-1
plt.axvline(x=1794, ls=':', color='black', ymax = 0.75) #line showing: x = 1800cm-1
plt.axvline(x=2512, ls=':', color='black', ymax = 0.6) #line showing: x = 2512cm-1

#Carbon dioxide
plt.axvline(x=2349, ls=':', color='black', ymax = 0.4) #doublet indicating the presence o
f CO2
#-----
#Plot details
plt.xlabel('Wavenumber [cm-1]', fontsize=15, labelpad = 15) #labe; x-axis
plt.ylabel('PAS Intensity [arb.units]', fontsize=15, labelpad = 15) #label y-axis
plt.xticks(fontsize=16) #Fontsize of x-axis t
icks
plt.yticks(fontsize=16) #Fontsize of y-axis t
icks
plt.legend(loc='upper left' ,fontsize=16) #legend
plt.axis([4000,400,-0.0025,0.011]); #axis range: [(xmax,m
xin,ymin,ymax)]

```

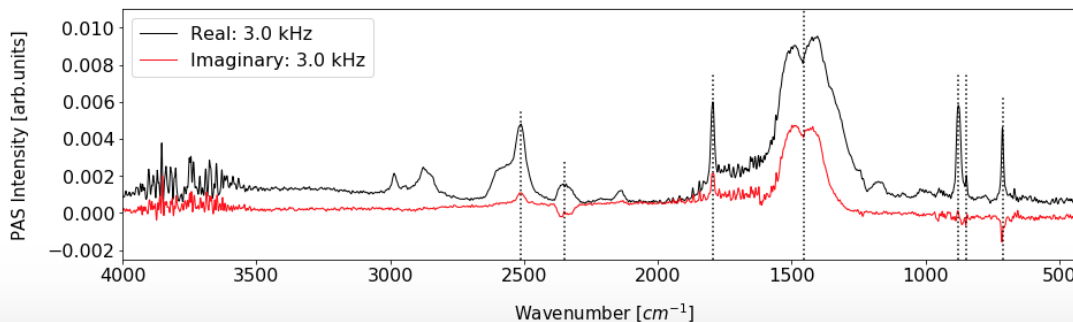


Figure A.1: Computational notebook containing python code employed in this work.

# Appendix B

## Sign Change of Peaks

As discussed in Section 3.9 , normalizing the peak intensities helped us analyze whether the widths and positions of the peaks were changing as the scan frequency was increased. The results for each individual peak are displayed in Figures B.1 for the real component spectra and Figure B.2 for the imaginary component spectra. Peak width and peak position are unchanged in both component spectra. This is also true for peaks with very low signal-to-noise ratios, such as the  $\nu_1 + \nu_3$  and  $\nu_1 + \nu_4$  peaks. However, changes in the  $\nu_3$  are visible and significant. The answers to what these changes mean go beyond the scope of this thesis' study and will require a closer examination.

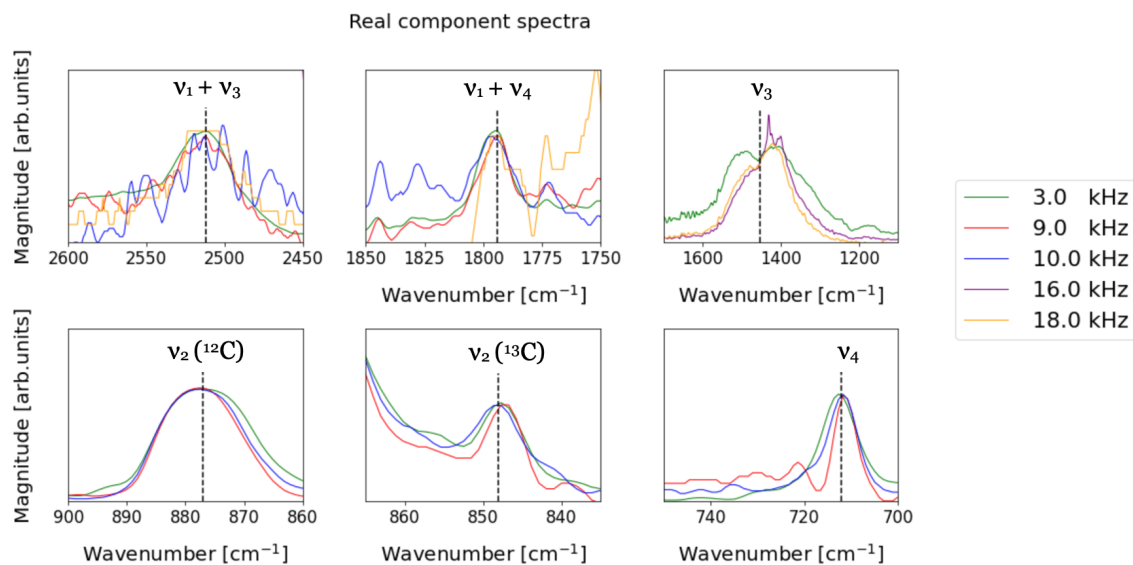


Figure B.1: Magnitude spectra for each vibrational mode in the real component spectra.

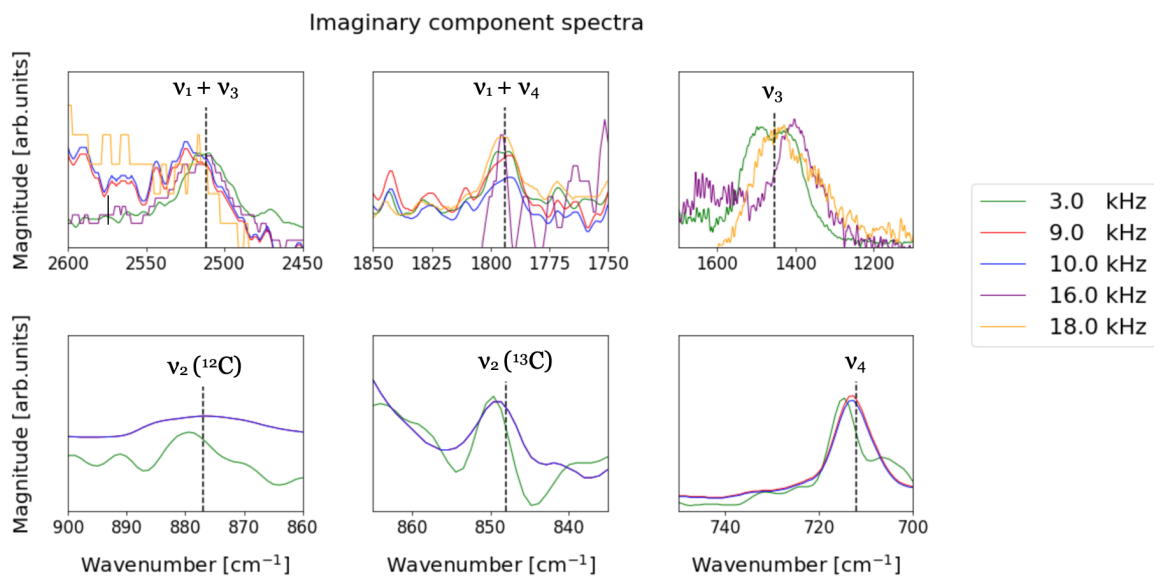


Figure B.2: Magnitude spectra for each vibrational mode in the imaginary component spectra.

# Bibliography

- [1] A. G. Bell. Lxviii. upon the production of sound by radiant energy. *The London, Edinburgh, and Dublin Philosophical Magazine and Journal of Science*, 11:510–528, 1881.
- [2] S. Campbell. Development of idealized practices for photoacoustic spectroscopy. Master's thesis, St. John's, Newfoundland, 2017.
- [3] S. Campbell, M. Dusseault, B. Xu, K. H. Michaelian, and K. M. Poduska. Supplemental material for photoacoustic detection of weak absorption bands in infrared spectra of calcite. *in press*, in press:in press, 2020.
- [4] J. Demšar, T. Curk, A. Erjavec, Črt Gorup, T. Hočevar, M. Milutinovič, M. Možina, M. Polajnar, M. Toplak, A. Starič, M. Štajdohar, L. Umek, L. Žagar, J. Žbontar, M. Žitnik, and B. Zupan. Orange: Data mining toolbox in python. *Journal of Machine Learning Research*, 14:2349–2353, 2013.
- [5] M. Dusseault. Photoacoustic infrared spectroscopy of calcite and aragonite and the effects of cell resonance on spectra. B.s. thesis, Memorial University of Newfoundland, St. John's, Newfoundland, 2018.
- [6] B. O. Ettlingen. Spectroscopic software: Opus reference manual. Available at [ftp://ftp.gps.caltech.edu/pub/tccon/tccon{\\\_}manuals{\\\_}and{\\\_}documentation/IFS125/0PUS{\\\_}Manual.pdf](ftp://ftp.gps.caltech.edu/pub/tccon/tccon{\_}manuals{\_}and{\_}documentation/IFS125/0PUS{\_}Manual.pdf). Online; accessed (2020/9/08).
- [7] LibreTexts. Infrared: Interpretation. Available at <https://chem.libretexts.org/@go/page/1846>. Online; accessed (2021/01/16).
- [8] J. McClelland, R. Jones, S. Luo, and L. Seaverson. A practical guide to ftir photoacoustic spectroscopy. In D. P. B. Coleman, editor, *A practical Guide to Photoacoustic Spectroscopy*. CRC Press, P.O. Box 1095, Ames, IA 50014 USA, 03 1992.
- [9] J. F. McClelland, R. W. Jones, and S. Luo. Practical analysis of polymers with depth varying compositions using fourier transform infrared photoacoustic spectroscopy (plenary). *Review of Scientific Instruments*, 74:285–290, 2003.

- [10] K. H. Michaelian. Invited article: Linearization and signal recovery in photoacoustic infrared spectroscopy. *Review of Scientific Instruments*, 78:051301, 2007.
- [11] C. D. Porter and D. B. Tanner. Correction of phase errors in fourier spectroscopy. *International Journal of Infrared and Millimeter Waves*, 4:273–298, 1983.
- [12] A. Rosencwaig and A. Gersho. Theory of the photoacoustic effect with solids. *Journal of Applied Physics*, 47:64–69, 1976.
- [13] B. Xu, K. M. Poduska, and L. Kronik. Vibrational properties of isotopically enriched materials: the case of calcite. *RSC Advances*, 8:33985–33992, 2018.
- [14] B. Xu and K. M. Poduska. Linking crystal structure with temperature-sensitive vibrational modes in calcium carbonate minerals. *Phys. Chem. Chem. Phys.*, 16:17634–17639, 2014.